applied sciences

MDPI

*Article*

# Metrology of Nanostructures by Tomographic Mueller-Matrix Scatterometry

**Chao Chen, Xiuguo Chen *, Yating Shi, Honggang Gu, Hao Jiang and Shiyuan Liu ***

State Key Laboratory for Digital Manufacturing Equipment and Technology, Huazhong University of Science and Technology, Wuhan 430074, China; chaochen@hust.edu.cn (C.C.); yatingshi@hust.edu.cn (Y.S.); hongganggu@hust.edu.cn (H.G.); hjiang@hust.edu.cn (H.J.)

* Correspondence: xiuguochen@hust.edu.cn (X.C.); shyliu@hust.edu.cn (S.L.)


Received: 16 November 2018; Accepted: 10 December 2018; Published: 12 December 2018

**Abstract:** The development of necessary instrumentation and metrology at the nanoscale, especially fast, low-cost, and nondestructive metrology techniques, is of great significance for the realization of reliable and repeatable nanomanufacturing. In this work, we present the application of a homemade novel optical scatterometer called the tomographic Mueller-matrix scatterometer (TMS), for the measurement of photoresist gratings. The TMS adopts a dual rotating-compensator configuration and illuminates the nanostructure sequentially under test conditions by a plane wave, with varying illumination directions and records. For each illumination direction, the polarized scattered field along various directions of observation can be seen in the form of scattering Mueller matrices. That more scattering information is collected by TMS than conventional optical scatterometry ensures that it achieves better measurement sensitivity and accuracy. We also show the capability of TMS for determining both grating pitch and other structural parameters, which is incapable by current zeroth-order methods such as reflectometry- or ellipsometry-based scatterometry.

**Keywords:** ellipsometry; scatterometry; Mueller matrix; diffraction grating; inverse scattering; pitch measurement

## 1. Introduction

Nanomanufacturing involves manufacturing of products (including materials, structures, devices, and systems) with feature dimensions at the nanoscale [1]. It is an essential bridge between the newest nanoscience discoveries and real-world nanotechnology products. One critical challenge to the realization of nanomanufacturing is the development of the necessary metrology at the nanoscale [2]. Although scanning electron microscopy (SEM), atomic force microscopy (AFM), and transmission electron microscopy (TEM) have the ability to analyze extremely small targets, they are faced with high costs and throughput concerns, and are in general not well suited for integrated metrology applications.

In comparison with SEM, AFM, and TEM, optical scatterometry based on a reflectometer or an ellipsometer has become one of the most important techniques for measuring the critical dimension (CD) and overlay of nanostructures in semiconductor manufacturing, due to its inherent noncontact, nondestructive, time-effective, and relatively inexpensive merits [3–9]. It is different from conventional image-based metrology techniques, such as optical microscopy, in that the measurement in optical scatterometry is not a WYSIWYG (what you see is what you get) process and typically involves the solution of an inverse problem by fitting the measured data with a multiparameter model that describes the light-nanostructure interaction. Even so, it is not restricted by the well-known Abbe diffraction limit in image-based techniques and thus plays an important role in addressing devices with sub-wavelength feature sizes in the semiconductor industry.

With the ever-decreasing dimensions of advanced technology nodes (22 nm and beyond), there are also some challenges and limitations to optical scatterometry [10,11], such as the parameter correlation issue. In addition, optical scatterometry is mostly suitable for measuring repetitive dense structures, but infeasible for the measurement of isolated or generally non-periodic structures. To address the challenges or limitations in conventional optical scatterometry, several designs have been presented with the idea of trying to collect the scattering information about the nanostructure under test conditions as much as possible, such as with the goniometric optical scatter instrument [12–14], through-focus scanning optical microscopy [15], scatterfield microscopy [16], tomographic diffractive microscopy [17,18], and Fourier scatterometry [19,20]. Recently, we have also developed a novel instrument called the tomographic Mueller-matrix scatterometer (TMS) [21]. The TMS illuminates a sample sequentially by a plane wave with varying illumination directions (incidence angles $0^\circ$~$65.6^\circ$ and azimuthal angles $0^\circ$~$360^\circ$) and records. For each illumination direction, the polarized scattered filed along various directions of observation (scattering angles $0^\circ$~$67^\circ$ and azimuthal angles $0^\circ$~$360^\circ$) can be seen in form of scattering Mueller matrices. The experiments performed on a Si grating had preliminarily demonstrated the potential of a TMS in nanostructure metrology [21].

Due to the strong correlation between pitch and other structural parameters, it is a common practice to predetermine grating pitch by another metrology tool such as AFM, or directly fix grating pitch to its nominal value in the solution of the inverse problem in optical scatterometry. In this work, we present the application of a TMS for the accurate reconstruction of lithographic patterns. We show the capability of a TMS for determining both pitch and other structural parameters, which is incapable by current zeroth-order methods such as reflectometry- or ellipsometry-based scatterometry.

The rest of this paper is organized as follows. Section 2 briefly introduces the principle of the TMS. Section 3 presents the associated methods for determining pitch and other structural parameters by TMS. Section 4 first describes the sample under measurement and then provides the details of measurement results by TMS. Finally, we draw some conclusions in Section 5.

## 2. Experimental Setup

Figure 1 presents the scheme of the developed TMS, which is a combination of a Mueller matrix ellipsometer (MME) [22] and a reflection microscope. As shown in Figure 1, a broadband white light from a light source (LS; LDLS$^{TM}$, EQ-99FC, Energetiq, Woburn, MA, USA) is collimated by a flat convex lens (CL) and then filtered to be a monochromatic light by a bandpass filter (BF; FL632.8-1, Thorlabs, Inc., , Newton, NJ, USA). After reflected by a rotatable flat mirror (M), which functions as a scanner of illumination directions, the light beam passes through a polarization state generator (PSG) made up of a polarizer (P; PGT5012, Union Optic, Inc., Wuhan, China) and an optimally designed zero-order quartz crystal waveplate ($C_{r1}$). Then, a non-polarizing beam splitter (BS) and an achromatic doublet ($L_1$) guides light rays to be focused on the back focal plane (BFP) of a high numerical-aperture (NA) objective lens (OB; EC Epiplan-Apochromat 50×/0.95 HD DIC, Zeiss, Inc., Oberkochen, Germany). The emerging light from the BFP of the OB is then parallelly incident upon the sample. Afterwards, the scattered light from the sample successively traverses the OB, $L_1$, BS, a polarization state analyzer that consists of the same polarization components as a PSG but in a reverse order, another achromatic doublet ($L_2$), and is finally collected by a detector (D; PCO.edge 5.5, PCO, Inc., Kelheim, Germany).

As presented in the inset of Figure 1, the position of the focal point of the light beam on the BFP of the OB can be changed by rotating the flat mirror M, which further leads to the change of illumination direction on the sample. An epi-illumination setup is designed to collect the scattered-field distribution associated with each illumination direction by imaging the BFP of the OB. Thanks to the dual rotating-compensator configuration, a $4 \times 4$ Mueller matrix associated with each point on the BFP of the OB can be obtained. Since the 16 elements of a Mueller matrix contain all polarization information that one can extract from a linear polarization scattering process, the full polarization properties of the scattered field are thus achieved.

As for the Mueller matrix measurement, the Stokes vector $\boldsymbol{S}_{\text{out}}$ of the light beam detected by the detector can be expressed as the following Mueller matrix product with incident Stokes vector $\boldsymbol{S}_{\text{in}}$ [8,22]:

$$\begin{aligned} S_{\text{out}} = & [\mathbf{M}_{\text{A}}\mathbf{R}(A_0)][\mathbf{R}(-C_{20})\mathbf{M}_{\text{C2}}(\delta_2)\mathbf{R}(C_{20})][\mathbf{M}_{\text{t}}^{\text{BS}}\mathbf{M}_{\text{b}}^{\text{OB}}\mathbf{M}_{\text{S}}\mathbf{M}_{\text{f}}^{\text{OB}}\mathbf{M}_{\text{r}}^{\text{BS}}] \\ & \times[\mathbf{R}(-C_{10})\mathbf{M}_{\text{C1}}(\delta_1)\mathbf{R}(C_{10})][\mathbf{R}(-P_0)\mathbf{M}_{\text{P}}]S_{\text{in}}, \end{aligned} \tag{1}$$

where $\mathbf{M}_{\text{P}}$, $\mathbf{M}_{\text{C1}}(\delta_1)$, $\mathbf{M}_{\text{C2}}(\delta_2)$, and $\mathbf{M}_{\text{A}}$ are the Mueller matrices of the polarizer P, the first compensator $\text{C}_{\text{r1}}$, the second compensator $\text{C}_{\text{r2}}$, and the analyzer A; $M_r^{BS}$ and $M_t^{BS}$ are reflection and transmission matrices of the BS, respectively. $M_f^{OB}$ and $M_b^{OB}$ represent Mueller matrices of the OB in the illumination and collection directions, respectively. $\mathbf{M}_{\text{S}}$ is the sample Mueller matrix; $\mathbf{R}(\cdot)$ is the Mueller rotation transformation matrix for rotation by an angle, which can be the initial transmission-axis orientations of the polarizer and analyzer, $P_0$ and $A_0$, the initial fast-axis orientations of the 1st and 2nd rotating compensators, $C_{10}$ and $C_{20}$. $\delta_1$ and $\delta_2$ are the phase retardances of 1st and 2nd compensators, respectively. Details about the calibration of $P_0$, $A_0$, $C_{10}$, $C_{20}$, $\delta_1$ and $\delta_2$, as well as $M_r^{BS}$, $M_t^{BS}$, $M_f^{OB}$ and $M_b^{OB}$ can be found in Ref. [21] and are omitted here for the sake of brevity.

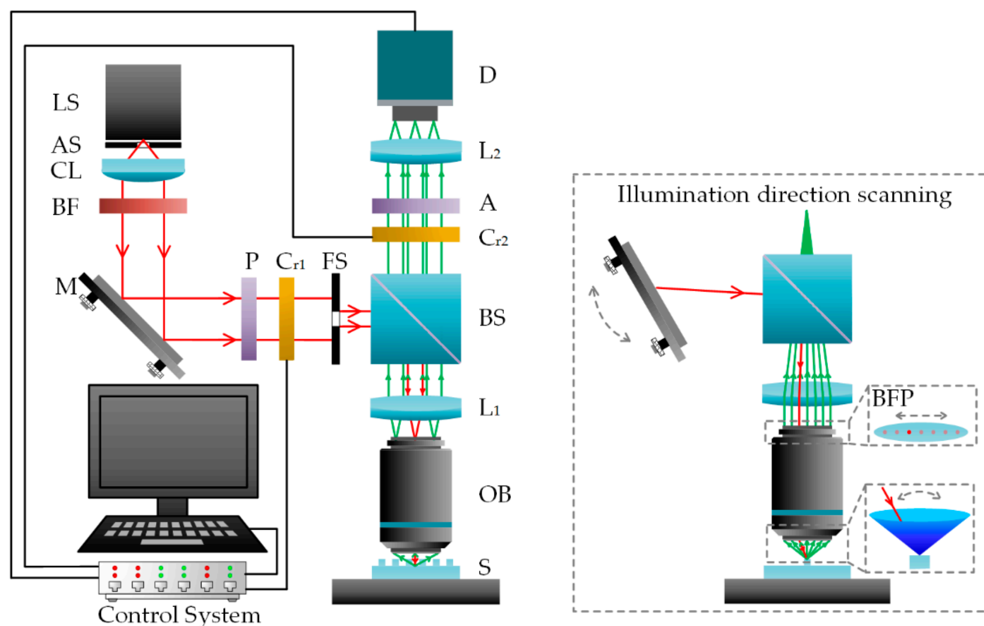


**Figure 1.** Scheme of the tomographic Mueller-matrix scatterometer (TMS). LS, light source; AS, aperture stop; CL, collimated lens; BF, bandpass filter; M, mirror; P and A, polarizer and analyzer; $\text{C}_{\text{r1}}$ and $\text{C}_{\text{r2}}$, 1st and 2nd rotating compensators; FS, field stop; BS, Beam splitter; $\text{L}_1$ and $\text{L}_2$, imaging lenses; OB, objective lens; S, sample; D, detector. The inset on the right side illustrates the principle of illumination direction scanning.

## 3. Methods

### 3.1. Inverse Modeling

The inverse modeling includes the solution of a direct problem and an indirect problem. The direct problem involves the establishment of a model to simulate the theoretical Mueller matrices of a nanostructure. The indirect problem involves the reconstruction of the nanostructure profile with the objective of finding an optimal input to the above established model whose simulated Mueller matrices can best match the measured values.

As for the direction problem here, the rigorous coupled-wave analysis (RCWA) [23,24] is used to simulate theoretical Mueller matrices of a periodic nanostructure. Figure 2 shows the case of polarized light incidence for a one-dimensional grating structure. The grating is denoted by vector

$\mathbf{x} = [x_1, x_2, \ldots, x_n]^T$ where $x_1, x_2, \ldots, x_n$ represent structural parameters such as top CD, height, sidewall angle, and so on. As shown in Figure 2b, the grating is divided by several different layers with boundaries joined together. Inverse modeling includes three steps: (1) derive electromagnetic expression from Maxwell's equations; (2) expand the permittivity function and electromagnetic fields into Fourier series; (3) and match the tangential field components at boundaries between different layers, reducing the boundary-value problem to an algebraic problem. According to the reflection coefficients calculated by solving the algebraic problem, a 2 × 2 Jones matrix **J** associated with the diffracted light can be formulated by:

$$\begin{bmatrix} E_{rp} \\ E_{rs} \end{bmatrix} = \mathbf{J}(\mathrm{x}) \begin{bmatrix} E_{ip} \\ E_{is} \end{bmatrix} = \begin{bmatrix} r_{pp} & r_{ps} \\ r_{sp} & r_{ss} \end{bmatrix} \begin{bmatrix} E_{ip} \\ E_{is} \end{bmatrix}, \tag{2}$$

where $E_{\mathrm{s,p}}$ refers to the electric field component perpendicular and parallel to the plane of incidence, respectively. When depolarization could be ignored, the Mueller matrix of the sample can be obtained by:

$$\mathbf{M} = \mathbf{A}(\mathbf{J} \otimes \mathbf{J}^*)\mathbf{A}^{-1}, \tag{3}$$

where the symbol ⊗ denotes the Kronecker product. $\mathbf{J}^*$ is the complex conjugate of **J**, and the matrix **A** is given by:

$$\mathbf{A} = \begin{bmatrix} 1 & 0 & 0 & 1 \\ 1 & 0 & 0 & -1 \\ 0 & 1 & 1 & 0 \\ 0 & \mathrm{i} & -\mathrm{i} & 0 \end{bmatrix}. \tag{4}$$

when depolarization could not be ignored, the sample Mueller matrix can be represented as the sum of multiple non-depolarizing Mueller matrices $\mathbf{M} = \sum_i M_i$, and each non-depolarizing Mueller matrices can be calculated as mentioned above [25]. In practice, the Mueller matrix **M** is usually normalized to the (1, 1)th element $M_{11}$, with the */normalized Mueller matrix elements being $m_{ij} = M_{ij}/M_{11}$.

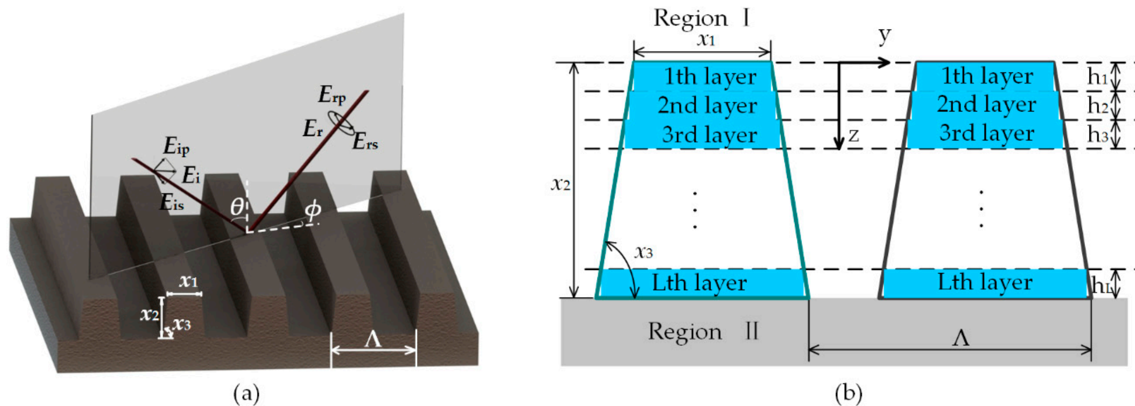


**Figure 2.** (**a**) Representation of polarized light incidence for a one-dimensional grating; (**b**) layers division in inverse modeling using rigorous coupled-wave analysis.

As for the indirect problem, a weighted least-squares regression analysis (Levenberg-Marquardt algorithm [26]) is performed, during which the structural parameters under measurement are varied until the calculated and measured data match as close as possible. This is done by minimizing a weighted mean square function $\chi_r^2$ defined by:

$$\chi_r^2 = \frac{1}{15N - P} \sum_{k=1}^{N} \sum_{j=1}^{4} \left[ \frac{m_{ij,k}^{\exp} - m_{ij,k}^{calc}(\mathbf{x})}{\sigma(m_{ij,k})} \right]^2, \tag{5}$$

where $k$ indicates the $k$th data point, which could be a wavelength, incidence angle, or azimuthal angle point. From the total number $N$, indices $i$ and $j$ show all the Mueller matrix elements except $m_{11}$ (normalized to $m_{11}$). $m_{ij,k}^{exp}$ denotes the Mueller matrix elements measured with the standard deviation of $\sigma(m_{ij,k})$, and $m_{ij,k}^{calc}(\mathbf{x})$ denotes the calculated Mueller matrix elements associated with the vector $\mathbf{x}$. Since the Levenberg-Marquardt algorithm is apt to fall into local minima, proper starting values for the fitting parameters are required in the iteration, which are usually taken as their nominal values or as the SEM-measured values if available. In addition, the curve of $\chi_r^2$ in a small parameter range centered on the extracted parameter values is usually plotted to check the uniqueness of the minimal point, to ensure that the found solution is the globally optimum solution.

### 3.2. Pitch Measurement

In scatterometric data analysis, the grating pitch is commonly fixed to extract other profile parameters. However, inaccurate pitch values would lead to a poor result. Moreover, it is difficult to set the pitch dimension Λ as a parameter, because it is coupled with other parameters which may make measurements imprecise. Next, we show how to measure grating pitch by TMS.

For grating periods Λ larger than λ/2, where λ is the wavelength of the incident light, the first-order diffracted light can be easily observed at an emergent angle $\theta$. Assuming $\vartheta$ is the difference between the diffraction angles of the zeroth- and first-order diffracted light, according to the grating equation the grating pitch can be written as:

$$\Lambda = \frac{\lambda}{\sin\vartheta\cos\theta + (1 - cos\vartheta)sin\theta}. \tag{6}$$

It is easy to see the variable $\vartheta$ become the only parameter to measure pitch. There are three ways to obtain the value of $\vartheta$. The first one is a so-called Littrow configuration [27]. The schematic drawing of the method is presented in Figure 3. The main point is to rotate the grating to ensure the incidence light coincides with the first-order diffracted light. Assumed rotating angle of the grating is $\alpha$, then it is simple to know $\vartheta = 2\alpha$ and $\theta = 90^\circ - \alpha$. Equation (6) could be rewritten as:

$$\Lambda = \frac{\lambda}{2\sin\alpha}. \tag{7}$$

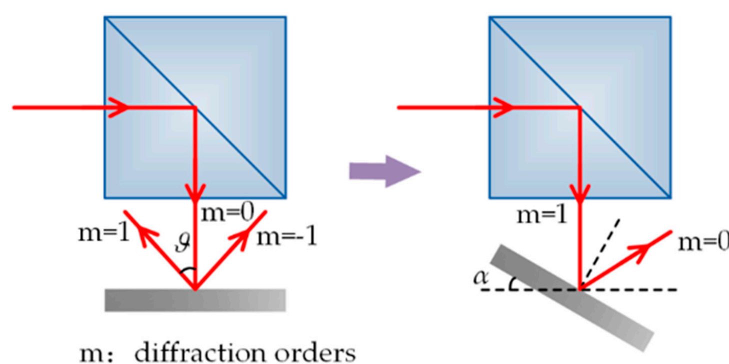


**Figure 3.** Littrow configuration for grating pitch measurement.

The second method is to use a grating whose pitch is known as a reference. Because a camera is used as a detector, the number of pixels can be acquired between the zeroth- and first-order diffracted light spot projected on the camera, set as $d_1$ and $d_2$ for reference and sample grating, respectively. Next, we can calculate the difference of diffraction angles $\vartheta_1$ and angle of zeroth-order diffracted light $\beta_0$, which is equal to the incidence angle $\theta$, using the grating equation. When the sample grating

is illuminated by the same incidence light, $\beta_0$ is same to that of the reference one. Afterwards, the difference of diffraction angles $\vartheta_2$ for simple grating can be obtained through the geometric relation:

$$\frac{\tan\vartheta_2 - \tan\beta_0}{\tan\vartheta_1 - \tan\beta_0} = \frac{d_2}{d_1}. \tag{8}$$

In case of the influence of aberrations of the optical system, test targets such as concentric circle and crosshair grid targets are used to calibrate and compensate errors induced by the system. If there is no reference grating available, as a third method we could use two different lights whose wavelengths ($\lambda_1$ and $\lambda_2$) are known to illuminate sample grating at the same incidence angle. It is similar to the second method, thus there is no more detailed description. For this case, another geometric relation is:

$$\frac{\sin(\vartheta'_2 + \beta_0) + \sin\beta_0}{\sin(\vartheta'_1 + \beta_0) + \sin\beta_0} = \frac{\lambda_2}{\lambda_1}. \tag{9}$$

The intensity of diffracted light is recorded by the camera. However, for a real light beam, the diameter could not be extremely small, so on the camera there usually is a spot with several pixels. When we deal with the signal, the data from a pixel is chosen for analysis. For a practical optical system, there are inevitably aberrations and misplacements of optical components. Due to the asymmetrical intensity distribution, the pixel chosen would influence the result. Therefore, a pixel picked from a spot shouldn't be random. The approach is based on calculating the center of mass (COM),

$$p = \frac{\sum_{i=1}^{N}\sum_{j=1}^{M} iI_{ij}}{\sum_{i=1}^{N}\sum_{j=1}^{M} I_{ij}}, \qquad q = \frac{\sum_{i=1}^{N}\sum_{j=1}^{M} jI_{ij}}{\sum_{i=1}^{N}\sum_{j=1}^{M} I_{ij}}, \tag{10}$$

where $I_{ij}$ is the intensity of pixel $(i, j)$ in a $N \times M$ image, and $(p, q)$ is the COM of light spot.

## 4. Results and Discussion

### 4.1. Sample Description

The sample is a photoresist array on a bottom anti-reflective coating (BARC) layer deposited on a Si substrate. Figure 4 presents a cross-sectional SEM image of the photoresist grating structure. Nominal dimensions of the grating structure are as follows: grating pitch = 400 nm, top critical dimension $x_1$ = 200 nm, grating height $x_2$ = 311 nm, and sidewall angle $x_3$ = 90°. The SEM image indicates that the top corner rounding could not be ignored, while the bottom corner rounding is unnoticeable. Therefore, the top corner rounding denoted by parameter $x_4$ in Figure 4 is also taken into consideration. In data analysis, we fixed the grating pitch and let the parameters $x_1$~$x_4$ vary. As well, optical constants are necessary, and for the Si substrate, it was taken from literature [28]. The optical properties of the BARC layer were modeled using a Tauc-Lorentz model [29], the parameters of which were taken as $A$ = 6.4378 eV, $C$ = 0.609 eV, $E_0$ = 5.851 eV, $E_g$ = 4.914 eV, and a Gaussian model [30], parameters of which were taken as $A$ = 0.8567 eV, $\omega_0$ = 0.3174 eV, $\sigma$ = 6.429 eV, respectively. The optical properties of the resist layer were modeled using a Cody-Lorentz model [31], the parameters of which were taken as $A$ = 2.261 eV, $\Gamma$ = 0.750 eV, $E_0$ = 6.189 eV, $E_g$ = 4.867 eV, $E_t$ = 0.292 eV, $E_u$ = 2.000 eV, and three Lorentz models [32], the parameters of which were taken as $A$ = 0.7089 eV, 0.1628 eV, 0.1755 eV, $\Gamma$ = 0.3315 eV, 0.2055 eV, 0.3886 eV, $E_n$ = 5.414 eV, 4.404 eV, 4.786 eV, respectively. Both the BARC and photoresist layers were predetermined by a commercial MME (ME-L, Eoptics Technology Co., Wuhan, China), which can provide full 4 × 4 Mueller matrices in the spectral range of 200–1000 nm.

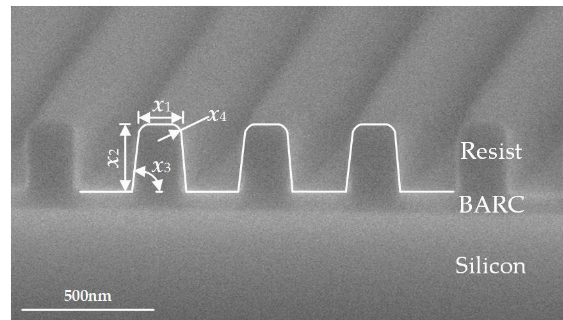


**Figure 4.** SEM micrograph and geometric model of the photoresist grating.

### 4.2. Measurement of the Grating Pitch

We used the Littrow configuration method to measure the grating pitch by TMS. We set the incidence angle at $\theta = 0°$, thus the zeroth-order diffracted light is overlapped with the incidence light. Then, the sample stage was rotated so that the zeroth-order diffraction light deflected from its initial direction and the first-order diffracted light coincided with the incident light. The rotating angle of the stage was 50.2°, and the illumination wavelength used was 633 nm. Substituting the values into Equation (7), and the calculated pitch of the grating is about 412 nm, which is in good agreement with the SEM-measured pitch value of about 414 nm from Figure 4.

As described in Section 3.2, the Littrow configuration method is applicable when the grating pitch is greater than $\lambda/2$. In our case, for a wavelength $\lambda$ = 633 nm, the grating pitch cannot be less than 316.5 nm. To further extend the range of pitch measurement, a shorter wavelength is required. A bandpass filter with a 1 nm bandwidth (FL632.8-1, Thorlabs, Inc., Newton, NJ, USA) was employed in the measurement to ensure an accurate result, since the diffracted light associated with different wavelengths within the bandwidth will be undistinguished on the detector for a bandpass filter with a small bandwidth. Additionally, it should be noted that in the measurements of different rotating angles of the sample stage will lead to a minor change of spot size, which will further lead to a change in the number of grating periods covered by the illumination spot in the pitch measurement.

### 4.3. Measurement of Grating Structural Parameters

To reduce errors caused by sample nonuniformity, the measurements of grating pitch and other structural parameters were carried out on the same grating region. Figure 5 presents the scattered field of the photoresist grating collected at the wavelength of 633 nm, the incidence angles varied from 0° to 65° at interval of 1°, azimuthal angles from 0° to 90° at interval of 5°. The reason why the azimuthal angle was limited to the range of 0°~90° rather than 0°~360° is that the Mueller matrices stay unchanged after a 180° rotation, due to rotation symmetry of the photoresist grating. The grating also has reflection symmetry relative to the plane that is perpendicular to the periodic direction. Since the photoresist grating sample is a periodic structure, the collected scattered field is actually a diffracted field. Due to the limitation of the NA of the objective lens in the TMS, for each illumination direction, only the zeroth-order diffracted light was collected. As shown in Figure 5, the panel associated with each Mueller matrix element consists of three sectorial parts, of which the lower right part corresponds to the TMS-measured data. The polar coordinate system of the sectorial part is set, as shown in the inset of Figure 5, with the radial coordinate being the sine of the incidence angle $\sin\theta$ and the angular coordinate being the azimuthal angle $\varphi$. As can be observed, as the azimuthal angles change, the grating exhibits anisotropy with the $2 \times 2$ off-diagonal Mueller matrix elements deviating from about 0 at $\varphi = 0°$, and finally approaching to about 0 when $\varphi = 90°$. We also calculated the depolarization index distribution associated with the TMS-measured data according to $DI = \sqrt{\left[\mathrm{Tr}(\mathbf{M}\mathbf{M}^{\mathrm{T}}) - m_{11}^2\right]/3m_{11}^2}$ $(0 \leq DI \leq 1)$ [33], with $DI = 1$ and $DI = 0$ representing a totally non-depolarizing and a totally depolarizing Mueller matrix, respectively. The calculated

depolarization indices indicated that $|DI - 1| < 0.028$, so the depolarization effect could be ignored in the following data analysis.

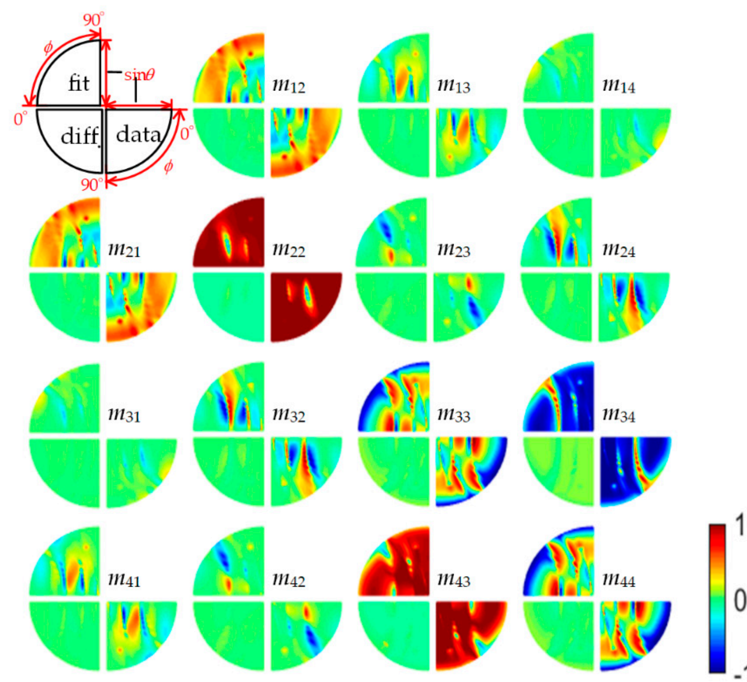


**Figure 5.** Mueller matrix representation of the zeroth-order diffracted field of the photoresist grating collected at the wavelength of 633 nm. The incidence angles varied from 0° to 65° at interval of 1°, and the azimuthal angles from 0° to 90° at interval of 5°. The panel associated with each Mueller matrix element (normalized to $m_{11}$) consists of three sectorial parts. The lower right part corresponds to the TMS-measured data, the upper left part corresponds to the calculated best-fit data, and the lower left part presents the difference between the measured and calculated best-fit data. For each sectorial part, the polar coordinate system is set as shown in the inset with the radial coordinate being the sine of the incidence angle sin$\theta$ and the angular coordinate being the azimuthal angle $\varphi$.

It should be noted that the angle-resolved Mueller polarimetry [34] can also acquire the diffracted field of a grating sample similar to the TMS. However, it should be pointed out that the measurement modes of the angle-resolved Mueller polarimetry and TMS are inherently different. For the angle-resolved Mueller polarimetry, polarization properties are acquired simultaneously by illuminating a sample simultaneously at all possible incidence angles and imaging the BFP of a high NA objective lens. When the sample is a periodic dense structure, both the TMS and angle-resolved Mueller polarimetry are appropriate for characterizing the sample. However, for a case in which the pitch of a periodic dense structure is greater than $\lambda/(2\times\text{NA})$, or an isolated or non-periodic structure is detected, an overlapping between the polarized scattering information occurs at the BFP of the objective lens in the angle-resolved Mueller polarimetry. In comparison, the TMS overcomes these limits and can distinguish information appropriately.

As shown in Figure 5, the upper left one of the three sectorial parts of each panel presents the calculated best-fit data to the TMS-measured data. To make it clear, the difference between the TMS-measured data and the calculated best-fit data is presented in the lower left sectorial part of each panel. It was found that the difference of most points was less than 0.02. To make a comparison, we also provided the results measured by the commercial MME. As an example, Figure 6 presents the fitting result of the measured and calculated best-fit Mueller matrices of the photoresist grating at the wavelength of 633 nm, the incidence angles varied from 50° to 65° at an interval of 1°, and the azimuthal angles of 50° and 60°. Good agreement can be observed from Figure 6. As can also be observed, the TMS-measured results exhibit good agreement with those measured by MME. Some deviations

between the TMS- and MME-measured data may be induced by measurement errors. Still, the different sizes and locations of illumination spots between TMS and MME may induce an unequal number of grating periods and different areas detected by the systems, bringing about little disparity in the measured results.

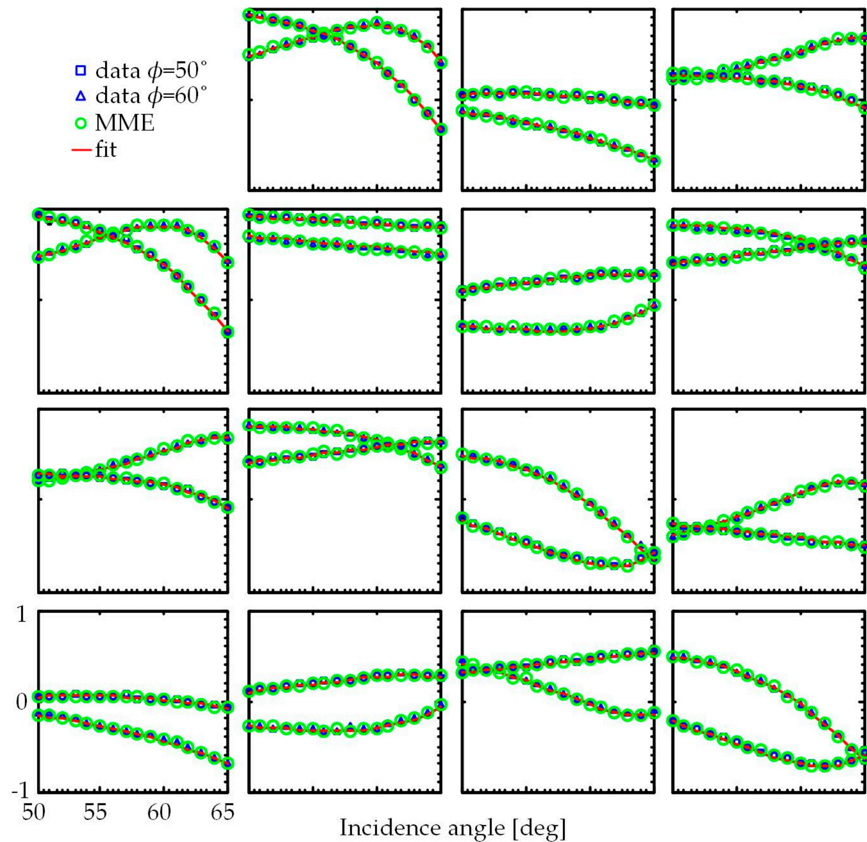


**Figure 6.** Fitting result of the measured and calculated best-fit Mueller matrices of the photoresist grating at the wavelength of 633 nm. The incidence angles varied from 50° to 65° at interval of 1°, and the azimuthal angles of 50° and 60°. The red solid lines represent the calculated best-fit data, the blue rectangles and blue triangles represent the TMS-measured data at the azimuthal angles of 50° and 65°, respectively. The green circles represent the corresponding MME-measured data for a comparison.

Table 1 presents the comparison of fitting parameters of the photoresist grating extracted from TMS, MME, and SEM measurements. For TMS measurements, we present both the fitting parameter values before and after the pitch correction. For MME measurements, we only present the fitting parameter values after the pitch correction. As can be seen, after the pitch correction, the TMS measured parameters $x_1$ and $x_3$ match well with their nominal values and MME and SEM results. As for the parameter $x_2$, the TMS-measured result exhibits a discrepancy with its nominal value and SEM result, but shows good agreement with the MME measured result. The top corner rounding $x_4$ also matches well with the MME result. This discrepancy is probably due to sample denaturation. We analyzed areas with structures and the assumption was supported by variations in the refractive index and extinction coefficient of the photoresist in comparison with our previous analysis [35]. A changed mixing layer existing between the resist and BARC layers could have introduced the measurement error. In addition, a possible modification of the structural cross-section due to the slicing process in SEM measurement (typically the focused ion beam), as well as the different testing areas of TMS and SEM on the sample, may be other reasons for the discrepancy. Even so, a noticeable improvement in accuracy of the extracted parameters can be recognized from the TMS-measured parameters before and

after the pitch correction. It is thereby necessary to acquire accurate pitch value before the extraction of other grating structural parameters, as it affects the results greatly.

**Table 1.** Comparison of the fitting parameters of the photoresist grating extracted from TMS, MME, and SEM measurements.

| Parameter | Nominal Value | TMS | | MME | SEM |
|---|---|---|---|---|---|
| | | Before Correction | After Correction | | |
| $x_1$ (nm) | 200 | 206.1 | 204.2 | 204.7 | 203.4 |
| $x_2$ (nm) | 311 | 343.5 | 295.8 | 294.5 | 303.7 |
| $x_3$ (deg) | 90 | 88.9 | 89.2 | 89.7 | 89.5 |
| $x_4$ (nm) | — | 53.3 | 54.3 | 52.1 | — |

## 5. Conclusions

In this work, we have presented the measurement of a photoresist grating by a homemade TMS. We have shown the collection of the polarized scattered-field distributions of the photoresist grating by TMS at different illumination directions. To reconstruct the grating profile parameters, an inverse scattering problem solving method has been adopted to fit the measured data with a RCWA model. The reconstructed grating profile parameters have exhibited good agreement with those measured by a commercial MME and SEM. In addition, the comparison between the TMS-measured results with and without pitch correction has also demonstrated the capability of TMS for determining both the grating pitch and other structural parameters, which is impossible with current zeroth-order methods such as reflectometry- or ellipsometry-based scatterometry, due to the strong correlation between pitch and other structural parameters in the solution of the inverse scattering problem.

**Author Contributions:** Conceptualization, X.C.; methodology and formal analysis, C.C. and X.C.; writing—original draft preparation, C.C.; writing—review and editing, X.C., Y.S., H.G., H.J., and S.L.; supervision, X.C. and S.L.; project administration, X.C. and S.L.; funding acquisition, X.C. and S.L.

**Funding:** This research was funded by the National Natural Science Foundation of China (Grant Nos. 51727809, 51775217, 51525502, and 51475191), the National Science and Technology Major Project of China (Grant No. 2017ZX02101006-004), and the National Science Foundation of Hubei Province of China (Grant Nos. 2018CFB559 and 2018CFA057).

**Acknowledgments:** The authors thank Shanghai Micro Electronics Equipment Co., Ltd. (Shanghai, China) for preparing the grating sample.

**Conflicts of Interest:** The authors declare no conflict of interest.

## References

1. Fang, F.Z.; Zhang, X.D.; Gao, W.; Guo, Y.B.; Byrne, G.; Hansen, H.N. Nanomanufacturing—Perspective and applications. *CIRP Ann. Manuf. Technol.* **2017**, *66*, 683–705. [CrossRef]
2. Postek, M.T.; Lyons, K. Instrumentation, metrology, and standards: Key elements for the future of nanomanufacturing. *Proc. SPIE* **2007**, *6648*, 664802.
3. Raymond, C.J. Scatterometry for semiconductor metrology. In *Handbook of Silicon Semiconductor Metrology*; Diebold, A.C., Ed.; CRC Press: Boca Raton, FL, USA, 2001; Chapter 18.
4. Huang, H.T.; Kong, W.; Terry, F.L., Jr. Normal-incidence spectroscopic ellipsometry for critical dimension monitoring. *Appl. Phys. Lett.* **2001**, *78*, 3983–3985. [CrossRef]
5. Wurm, M.; Endres, J.; Probst, J.; Schoengen, M.; Diener, A.; Bodermann, B. Metrology of nanoscale grating structures by UV scatterometry. *Opt. Express* **2017**, *25*, 2460–2468. [CrossRef] [PubMed]
6. Novikova, T.; De Martino, A.; Bulkin, P.; Nguyen, Q.; Drévillon, B.; Popov, V.; Chumakov, A. Metrology of replicated diffractive optics with Mueller polarimetry in conical diffraction. *Opt. Express* **2007**, *15*, 2033–2046. [CrossRef] [PubMed]
7. Kim, Y.N.; Paek, J.S.; Rabello, S.; Lee, S.; Hu, J.; Liu, Z.; Hao, Y.; McGahan, W. Device based in-chip critical dimension and overlay metrology. *Opt. Express* **2009**, *17*, 21336–21343. [CrossRef] [PubMed]

8. Liu, S.; Chen, X.; Zhang, C. Development of a broadband Mueller matrix ellipsometer as a powerful tool for nanostructure metrology. *Thin Solid Films* **2015**, *584*, 176–185. [CrossRef]
9. Diebold, A.C.; Antonelli, A.; Keller, N. Perspective: Perspective: Optical measurement of feature dimensions and shapes by scatterometry. *APL Mater.* **2018**, *6*, 058201. [CrossRef]
10. Bundary, B.; Solecky, E.; Vaid, A.; Bello, A.F.; Dai, X. Metrology capabilities and needs for 7 nm and 5 nm logic nodes. *Proc. SPIE* **2017**, *10145*, 101450G.
11. Orji, N.G.; Badaroglu, M.; Barnes, B.M.; Beitia, C.; Bunday, B.D.; Celano, U.; Kline, R.J.; Neisser, M.; Obeng, Y.; Vladar, A.E. Metrology for the next generation of semiconductor devices. *Nat. Electron.* **2018**, *1*, 532–547. [CrossRef]
12. Germer, T.A.; Asmail, C.C. Goniometric optical scatter instrument for out-of-plane ellipsometry measurements. *Rev. Sci. Instrum.* **1999**, *70*, 3688–3695. [CrossRef]
13. Liu, C.Y.; Liu, T.A.; Fu, W.E. Out-of-plane ellipsometry measurements of nanoparticles on surfaces for thin film coated wafer inspection. *Opt. Laser Technol.* **2010**, *42*, 902–910. [CrossRef]
14. Maria, J.; Aas, L.M.S.; Kildemo, M. In and out of incidence plane Mueller matrix scattering ellipsometry of rough mc-Si. *Thin Solid Films* **2014**, *571*, 399–404. [CrossRef]
15. Attota, R.; Germer, T.A.; Silver, R.M. Through-focus scanning-optical-microscope imaging method for nanoscale dimensional analysis. *Opt. Lett.* **2008**, *33*, 1990–1992. [CrossRef] [PubMed]
16. Silver, R.M.; Barnes, B.M.; Attota, R.; Jun, J.; Stocker, M.; Marx, E.; Patrick, H.J. Scatterfield microscopy for extending the limits of image-based optical metrology. *Appl. Opt.* **2007**, *46*, 4248–4257. [CrossRef] [PubMed]
17. Maire, G.; Drsek, F.; Girard, J.; Giovannini, H.; Talneau, A.; Konan, D.; Belkebir, K.; Chaumet, P.C.; Sentenac, A. Experimental demonstration of quantitative imaging beyond Abbe's limit with optical diffraction tomography. *Phys. Rev. Lett.* **2009**, *102*, 213905. [CrossRef] [PubMed]
18. Zhang, T.; Ruan, Y.; Maire, G.; Sentenac, D.; Talneau, A.; Belkebir, K.; Chaunet, P.C.; Sentenac, A. Full-polarized tomographic diffraction microscopy achieves a resolution about one-fourth of the wavelength. *Phys. Rev. Lett.* **2013**, *111*, 243904. [CrossRef] [PubMed]
19. Boher, P.; Petit, J.; Leroux, T.; Foucher, J.; Desieres, Y.; Hazart, J.; Chaton, P. Optical Fourier transform scatterometry for LER and LWR metrology. *Proc. SPIE* **2005**, *5752*, 594526.
20. Petrik, P.; Kumar, N.; Fried, M.; Fodor, B.; Urbach, H.P. Fourier ellipsometry—An ellipsometric approach to Fourier scatterometry. *J. Eur. Opt. Soc. Rapid* **2015**, *10*, 15002. [CrossRef]
21. Tan, Y.; Chen, C.; Chen, X.; Du, W.; Gu, H.; Liu, S. Development of a tomographic Mueller-matrix scatterometer for nanostructure metrology. *Rev. Sci. Instrum.* **2018**, *89*, 073702. [CrossRef]
22. Li, J.; Ramanujam, B.; Collins, R.W. Dual rotating compensator ellipsometry: Theory and simulations. *Thin Solid Films* **2011**, *519*, 2725–2729. [CrossRef]
23. Moharam, M.G.; Grann, E.B.; Pommet, D.A.; Gaylord, T.K. Formulation for stable and efficient implementation of the rigorous coupled-wave analysis of binary gratings. *J. Opt. Soc. Am. A* **1995**, *12*, 1068–1076. [CrossRef]
24. Li, L. Use of Fourier series in the analysis of discontinuous periodic structures. *J. Opt. Soc. Am. A* **1996**, *13*, 1870–1876. [CrossRef]
25. Chen, X.; Zhang, C.; Liu, S. Depolarization effects from nanoimprinted grating structures as measured by Mueller matrix polarimetry. *Appl. Phys. Lett.* **2013**, *103*, 151605. [CrossRef]
26. Press, W.H.; Teukolsky, S.A.; Vetterling, W.T.; Flannery, B.P. *Numerical Recipies: The Art of Scientific Computing*, 3rd ed.; Cambridge University Press: Cambridge, UK, 2007; Chapter 15.
27. Chernoff, D.A.; Buhr, E.; Burkhead, D.L.; Diener, A. Picometer-scale accuracy in pitch metrology by optical diffraction and atomic force microscopy. *Proc. SPIE* **2008**, *6922*, 69223J.
28. Herzinger, C.M.; Johs, B.; McGahan, W.A.; Woollam, J.A.; Paulson, W. Ellipsometric determination of optical constants for silicon and thermally grown silicon dioxide via a multi-sample, multi-wavelength, multi-angle investigation. *J. Appl. Phys.* **1998**, *83*, 3323–3336. [CrossRef]
29. Jellison, G.E., Jr.; Modine, F.A. Parameterization of the optical functions of amorphous materials in the interband region. *Appl. Phys. Lett.* **1996**, *69*, 371–373. [CrossRef]
30. Meneses, D.D.S.; Malki, M.; Echegut, P. Structure and lattice dynamics of binary lead silicate glasses investigated by infrared spectroscopy. *J. Non-Cryst. Solids* **2006**, *352*, 769–776. [CrossRef]

31. Ferlauto, A.S.; Ferreira, G.M.; Pearce, J.M.; Wronski, C.R.; Collins, R.W.; Deng, X.; Ganguly, G. Analytical model for the optical functions of amorphous semiconductors from the near-infrared to ultraviolet: Applications in thin film photovoltaics. *J. Appl. Phys.* **2002**, *92*, 2424–2436. [CrossRef]
32. Synowicki, R.A. Spectroscopic ellipsometry characterization of indium tin oxide film microstructure and optical constants. *Thin Solid Films* **1998**, *313*, 394–397. [CrossRef]
33. Gil, J.J.; Bernabeu, E. Depolarization and polarization indices of an optical system. *Opt. Acta Int. J. Opt.* **1986**, *33*, 185–189. [CrossRef]
34. Ben Hatit, S.; Foldyna, M.; De Martino, A.; Drévillon, B. Angle-resolved Mueller polarimeter using a microscope objective. *Phys. Status Solidi A* **2008**, *205*, 743–747. [CrossRef]
35. Chen, X.; Du, W.; Yuan, K.; Chen, J.; Jiang, H.; Zhang, C.; Liu, S. Development of a spectroscopic Mueller matrix imaging ellipsometer for nanostructure metrology. *Rev. Sci. Instrum.* **2016**, *87*, 053707. [CrossRef] [PubMed]

© 2018 by the authors. Licensee MDPI, Basel, Switzerland. This article is an open access article distributed under the terms and conditions of the Creative Commons Attribution (CC BY) license (http://creativecommons.org/licenses/by/4.0/).